

Geometric Static Modeling Framework for Piecewise-Continuous Curved-Link Multi Point-of-Contact Tensegrity Robots

Lauren Ervin[✉], Student Member, IEEE, and Vishesh Vikas[✉], Member, IEEE

Abstract—Tensegrities synergistically combine tensile (cable) and rigid (link) elements to achieve structural integrity, making them lightweight, packable, and impact resistant. Consequently, they have high potential for locomotion in unstructured environments. This research presents geometric modeling of a Tensegrity eXploratory Robot (TeXploR) comprised of two semi-circular, curved-links held together by 12 prestressed cables and actuated with an internal mass shifting along each link. This design allows for efficient rolling with stability (e.g., tip-over on an incline). However, the unique design poses static and dynamic modeling challenges given the discontinuous nature of the semi-circular, curved-links, two changing points of contact with the surface plane, and instantaneous movement of the masses along the links. The robot is modeled using a geometric approach where the holonomic constraints confirm the experimentally observed four-state hybrid system, proving TeXploR rolls along one link while pivoting about the end of the other. It also identifies the quasi-static state transition boundaries that enable a continuous change in the robot states via internal mass shifting. This is the first time in literature a non-spherical two-point contact system is kinematically and geometrically modeled. Furthermore, the static solutions are closed-form and do not require numerical exploration of the solution. The MATLAB simulations are experimentally validated on a tetherless prototype with mean absolute error of 4.36° for the arc angles of the points of contact.

Index Terms—Automation, kinematics, space robotics.

I. INTRODUCTION

ROBOT locomotion in non-uniform terrains is a requirement for applications of space, search and rescue, and agriculture. Wheeled robots provide efficient and reliable locomotion in structured environments through continuity of contact with the surface. Their adaptation for unstructured environments include integration of legs [1] and introduction of discontinuity with compliance [2], [3]. Additionally, spherical robots have garnered interest due to the unique rolling locomotion and ability to rebound from collisions [4], [5], [6]. The curved-link tensegrity robot presented in this research brings together the best of both

Received 1 July 2024; accepted 6 October 2024. Date of publication 24 October 2024; date of current version 1 November 2024. This article was recommended for publication by Associate Editor G. Li and Editor G. Loianno upon evaluation of the reviewers' comments. This work was supported in part by NASA/Alabama Space Grant Consortium under Grant 80NSSC20M0044 and in part by USDA/NIFA under Grant 2023-67022-40918. (Corresponding author: Lauren Ervin.)

The authors are with the Agile Robotics Lab, University of Alabama, Tuscaloosa, AL 35487 USA (e-mail: lefaris@crimson.ua.edu; vvikas@ua.edu).

This letter has supplementary downloadable material available at <https://doi.org/10.1109/LRA.2024.3486199>, provided by the authors.

Digital Object Identifier 10.1109/LRA.2024.3486199

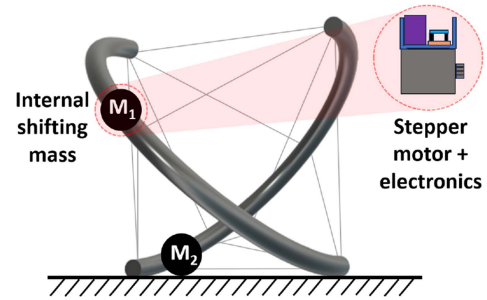


Fig. 1. Two curved-link tensegrity robot, TeXploR, is structurally held with 12 tensile cables. Change of robot pose is achieved through internal masses shifting along the links. At any instant, it has two points of contact with the ground.

worlds - discontinuities in wheel-designs, and locomotion ability of spherical robots.

The term tensegrity was introduced in the 1960s by Fuller and Snelson with initial applications in architecture [7]. Fundamentally, it combines rigid links under compression with prestressed cables held in tension to achieve structural integrity. As a result, they are lightweight, packable, and do not rely on gravity to maintain structural integrity [8]. Mobile tensegrity robots aim to leverage these advantages for locomotion in unstructured environments. Commonly, these robots are based on tensegrity primitives comprised of two, three, six, or 12 rigid, straight-links [9], [10], [11]. Locomotion with straight-links is discrete and results from shape change achieved by altering cable or link lengths [12]. Vibration-based locomotion has been explored by Rieffel et al. [13].

In contrast, curved-link robots adapt the rolling motion of a sphere, enabling energy efficient locomotion [14], [15], [16], [17]. The two curved-link robot [15] is about three times faster (normalized to body lengths/min) than the fastest straight-link counterpart. Here, the momentum change is achieved through internal mass shifting. This actuation methodology provides a greater ability of manipulating the momentum while minimizing the number of actuators, i.e., one moving mass per link opposed to linear actuators along cables and links. The presented research adopts a similar concept, shown in Fig. 1.

Despite the design advantages, the modeling of such a two-point contact system with piecewise continuity of the curved-links remains a challenge. For example, Böhm et al. [16] modeled the system where the robot performs uniaxial rolling about one end of the curved-link and the internal mass moves along a separate straight line connecting the two ends of a link. However, this non-geometric approach makes an assumption that the robot

pivots about the end of one link and rolls along the other, does not consider the masses of the curved-links, and the model is qualitatively validated. Kaufhold et al. [17] experimentally study the toppling locomotion of this robot where there is change in the point of pivot. Schorr et al. [18] also use an Euler angle approach to model the kinematics of a three curved-link robot capable of shape morphing. This approach, while effective, faces challenges with generalization and scaling, and does not provide insight into the hybrid nature of the robot that is experimentally observed. Antali et al. [19] propose an approach to model two point of contact locomotion of a sphere along two orthogonal planes similar to the edges of a wall. This letter addresses the mentioned shortcomings by adopting an elegant, generalizable, and scalable geometric modeling approach that proves the hybrid state of the robot and is experimentally validated.

Contributions: The letter statically models a mobile, curved-link tensegrity robot using a geometric representation and provides subsequent simulation and validation. The generalizable modeling framework is adaptable to robots with multiple points of contact and different morphologies. The model analytically proves the hybrid nature of the system where the robot exists in four states. Each state corresponds to the motion where the robot instantaneously pivots about the end of one curved-link and rolls along the other. Static simulations provide input-output relationship between internal mass positions and contact points, equivalently, the robot orientation. A tetherless robot prototype experimentally validates the static model with high accuracy.

Paper Organization: The next section explores the kinematics of the robot and proves its hybrid nature. The static modeling is analyzed in the following section. Thereafter, the fabrication and design methodology of the tensegrity robot is presented. Next, simulations with a scenario of state change along the transition boundaries for a quasi-static control path and real-world experimental results are discussed. The final section concludes the research and explores future directions.

II. ROBOT KINEMATICS

A. Problem Definition and Notation

The Tensegrity eXploratory Robot (TeXploR), Fig. 1, is comprised of two curved-links held together with a tensile cable and two motor assemblies that freely move along the links. The two links, $\{L_1, L_2\}$, are modeled as semi-circular arcs with radii r and masses $\{m_1, m_2\}$, shown in Fig. 2. The two endpoints of link L_i are denoted as $\{A_i, B_i\}$. For the remainder of this section, $i = 1, 2$ corresponding to the two links. The body coordinate system $\{b\}$ is fixed on the robot body with origin O_b and orthonormal basis $U_b = [\mathbf{x}_b, \mathbf{y}_b, \mathbf{z}_b] \in SO(3)$ where $SO(3) = \{U \in \mathbb{R}^{3 \times 3} : U^T U = I, \det U = +1\}$. Let coordinate systems $\{1, 2\}$ be fixed on the corresponding link with origin at the center of each arc, such that the x and z axes respectively are along the arc end points $B_i A_i$, and normal to the arc plane. The center of the two links are coincident and $\{1\}$ coincides with $\{b\}$. The inertial coordinate system $\{s\}$ is fixed at origin O_s with orthonormal basis $U_s = [\mathbf{x}_s, \mathbf{y}_s, \mathbf{z}_s] \in SO(3)$ such that \mathbf{z}_s is normal to the plane of locomotion. The motor assemblies are modeled as point masses M_i that move along the corresponding link. These point masses P_i are defined using angle θ_i from \mathbf{x}_i and denoted by $\mathbf{p}_i \in \mathbb{R}^{3 \times 1}$. The instantaneous points of contact, Q_i , between the links and the ground plane are represented by $\mathbf{q}_i \in \mathbb{R}^{3 \times 1}$ and parameterized using ground contact angles

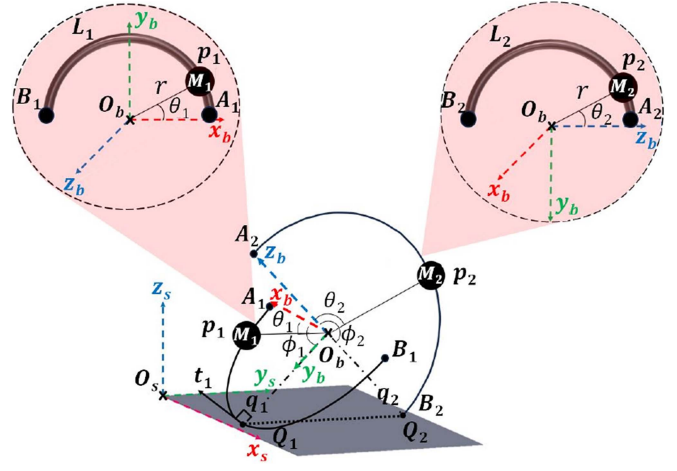


Fig. 2. Visualization of the inertial $\{s\}$ and body $\{b\}$ coordinate systems. Here, $\{b\}, \{1\}$ coincide and \mathbf{z}_s is normal to the ground plane. The internal masses P_i and contact points Q_i along the links are parameterized using θ_i, ϕ_i where $i = 1, 2$. The tangents at the contact points, t_i , lie along the surface.

TABLE I
SHIFTING MASSES AND POINTS OF CONTACT

Motor on link $i = 1, 2$		Point of contact along link $i = 1, 2$	
\mathbf{p}_i	Position vector	\mathbf{q}_i	Position vector
θ_i	Arc angle	ϕ_i	Arc angle
M_i	Motor mass	\mathbf{t}_i	Arc tangent at \mathbf{q}_i

ϕ_i from \mathbf{x}_i . The tangents of the arc at these instantaneous points of contact are denoted by $\mathbf{t}_i \in \mathbb{R}^{3 \times 1}$. Terminology of the shifting masses and points of contact is summarized in Table I. The rotation matrix, $R_{sb} \in SO(3)$, between the inertial and body coordinate systems can be defined using the principle that vectors are coordinate invariant, i.e., for a vector $\mathbf{v} \in \mathbb{R}^{3 \times 1}$

$$\mathbf{v} = U_s \mathbf{v}^s = U_b \mathbf{v}^b, \quad \mathbf{v}^s = R_{sb} \mathbf{v}^b, \text{ s.t. } R_{sb} = U_s^T U_b$$

where the superscript refers to the coordinate system of representation. Ultimately, it is desired to find the transformation matrix $T_{sb} \in SE(3)$ that changes the representation of a point in $\{b\}$ to $\{s\}$. For some point $\mathbf{p} \in \mathbb{R}^{3 \times 1}$

$$T_{sb} = \begin{bmatrix} R_{sb} & \mathbf{o}_{sb}^s \\ \mathbf{0}_{3 \times 1} & 1 \end{bmatrix}, \text{ s.t. } \begin{bmatrix} \mathbf{p}^s \\ 1 \end{bmatrix} = T_{sb} \begin{bmatrix} \mathbf{p}^b \\ 1 \end{bmatrix}$$

where \mathbf{o}_{sb} is the displacement between origins of $\{s\}, \{b\}$.

B. Kinematics

The position vectors $\mathbf{p}_i, \mathbf{q}_i$ are represented as a combination of the arc radius and respective angles along arcs.

$$\mathbf{p}_i^i = r \begin{bmatrix} c_{\theta_i} \\ s_{\theta_i} \\ 0 \end{bmatrix}, \quad \mathbf{q}_i^i = r \begin{bmatrix} c_{\phi_i} \\ s_{\phi_i} \\ 0 \end{bmatrix} \quad (1)$$

where $c_{\alpha_i} = \cos(\alpha_i), s_{\alpha_i} = \sin(\alpha_i), \forall i = 1, 2, \alpha = \theta, \phi$, and the superscript i refers to the coordinate system of representation. The transformation matrix $T_{12} \in SE(3)$ changes the representation of a point from coordinate system $\{2\}$

to $\{1\}$.

$$T_{12} = \begin{bmatrix} R_{12} & \mathbf{o}_{12}^1 \\ \mathbf{0}_{1 \times 3} & 1 \end{bmatrix}, R_{12} = \begin{bmatrix} 0 & 0 & 1 \\ 0 & -1 & 0 \\ 1 & 0 & 0 \end{bmatrix}, \mathbf{o}_{12}^1 = \begin{bmatrix} 0 \\ 0 \\ 0 \end{bmatrix} \quad (2)$$

where $R_{12} \in SO(3)$ and $\mathbf{o}_{12} \in \mathbb{R}^{3 \times 1}$ are the rotation matrix and the displacement between the origins of the $\{1\}$, $\{2\}$. Hence,

$$\begin{aligned} \mathbf{p}_1^b &= r \begin{bmatrix} c_{\theta_1} \\ s_{\theta_1} \\ 0 \end{bmatrix}, \quad \mathbf{p}_2^b = \mathbf{o}_{12} + R_{12}\mathbf{p}_2^2 = r \begin{bmatrix} 0 \\ -s_{\theta_2} \\ c_{\theta_2} \end{bmatrix} \\ \mathbf{q}_1^b &= r \begin{bmatrix} c_{\phi_1} \\ s_{\phi_1} \\ 0 \end{bmatrix}, \quad \mathbf{q}_2^b = \mathbf{o}_{12} + R_{12}\mathbf{q}_2^2 = r \begin{bmatrix} 0 \\ -s_{\phi_2} \\ c_{\phi_2} \end{bmatrix} \end{aligned} \quad (3)$$

The ‘free-vector’ tangent \mathbf{t}_i at points of contact Q_i are

$$\mathbf{t}_i = \frac{\partial \mathbf{q}_i}{\partial \phi_i} \quad (4)$$

C. Rolling Constraint

Pure rolling without slipping is assumed at the points of contact, Q_1, Q_2 . Hence, they have zero velocity, i.e., $\dot{\mathbf{q}}_1 = \dot{\mathbf{q}}_2 = 0$. We use the Lie group approach for modeling and follow the notation as per [20]. The body twist, $\xi_b \in \mathbb{R}^6$, encodes the angular velocity ω_b and linear velocity of the origin O_b , v_b . The hat operator $\hat{\cdot}$ maps $\mathbb{R}^{6 \times 1} \rightarrow \mathfrak{se}(3)$ and $\mathbb{R}^{3 \times 1} \rightarrow \mathfrak{so}(3)$

$$\xi_b = \begin{bmatrix} \omega_b \\ v_b \end{bmatrix}, \quad \hat{\xi}_b = \begin{bmatrix} \hat{\omega}_b & v_b \\ 0 & 0 \end{bmatrix} \in \mathfrak{se}(3)$$

The coordinate-free rolling constraint expressed in $\{b\}$ is

$$\dot{\mathbf{q}}_i = U_b(v_b + \hat{\omega}_b \mathbf{q}_i^b) = 0$$

In this letter, we restrict ourselves to static analysis and do not examine this constraint given the modeling complexity, especially, the hybrid nature of a two-point contact system.

D. Holonomic Constraint

It is assumed the robot is in physical contact with the ground surface at all times. This implies the two points Q_1, Q_2 and the tangents at those points lie on the ground plane. The ground plane is defined using the surface normal which is the z-axis \mathbf{z}_s of $\{s\}$. Another interpretation of this is that the \mathbf{z}_s component of position \mathbf{q}_i is the minimum amongst all the points on the link. For the two points of contact Q_i

$$[\mathbf{z}_s^T, 1] \cdot \left(T_{sb} \begin{bmatrix} \mathbf{q}_i \\ 1 \end{bmatrix} \right) = 0, \quad [\mathbf{z}_s^T, 1] \cdot \left(T_{sb} \begin{bmatrix} \mathbf{t}_i \\ 0 \end{bmatrix} \right) = 0 \quad (5)$$

This can be simplified to

$$\begin{aligned} \begin{bmatrix} (\mathbf{q}_1 - \mathbf{q}_2)^T \\ (\mathbf{t}_1)^T \\ (\mathbf{t}_2)^T \end{bmatrix} \mathbf{z}_s &= 0, \quad \text{where } \mathbf{z}_s^s = \begin{bmatrix} 0 \\ 0 \\ 1 \end{bmatrix} \\ \begin{bmatrix} (\mathbf{q}_1^b - \mathbf{q}_2^b)^T \\ (\mathbf{t}_1^b)^T \\ (\mathbf{t}_2^b)^T \end{bmatrix} \mathbf{z}_s^b &= 0, \quad \text{where } \mathbf{z}_s^b = R_{sb}^T \mathbf{z}_s^s \end{aligned} \quad (6)$$

Geometrically, this implies that vectors $(\mathbf{q}_1 - \mathbf{q}_2), \mathbf{t}_1, \mathbf{t}_2$ lie in the same plane with \mathbf{z}_s as the surface normal. The discontinuities at edges of the links, $\phi_i = 0, 180^\circ$, result in the tangents being undefined. Thus, the discontinuities result in three unique cases:

Case 1. Tangent vector \mathbf{t}_2 not defined: Here, vector \mathbf{z}_s is normal to the vector Q_1Q_2 and tangent vector at Q_1 . The direction of \mathbf{z}_s^b can be deduced from the fact that \mathbf{o}_{sb} , origin O_b of $\{b\}$ lies above the ground plane, i.e., $\mathbf{z}_s^T \mathbf{o}_{sb} > 0$, and Q_1, Q_2 are in contact with the ground. Mathematically,

$$\begin{aligned} (\mathbf{z}_s^s)^T (\mathbf{o}_{sb}^s + R_{sb} \mathbf{q}_i^b) &= 0, \text{ and } (\mathbf{z}_s^s)^T \mathbf{o}_{sb}^b > 0 \\ &\Rightarrow -(\mathbf{z}_s^b)^T \mathbf{q}_i^b > 0 \end{aligned}$$

The analytical solution for \mathbf{z}_s^b can then be summarized as

$$\begin{aligned} \mathbf{z}_s &= \pm \frac{\mathbf{t}_1 \times (\mathbf{q}_1 - \mathbf{q}_2)}{|\mathbf{t}_1 \times (\mathbf{q}_1 - \mathbf{q}_2)|} \text{ s.t. } -(\mathbf{z}_s)^T \mathbf{q}_1 = -(\mathbf{z}_s)^T \mathbf{q}_2 > 0 \\ \mathbf{z}_s^b &= \frac{-1}{\sqrt{2}} [c_{\phi_1}, s_{\phi_1}, c_{\phi_2}]^T, \quad -(\mathbf{z}_s^b)^T \mathbf{q}_1 = -(\mathbf{z}_s^b)^T \mathbf{q}_2 = \frac{r}{\sqrt{2}} \end{aligned} \quad (7)$$

Case 2. Tangent vector \mathbf{t}_1 not defined: Similar to the previous case, \mathbf{z}_s^b is normal to the vector Q_1Q_2 and the tangent vector at Q_2 . Using the surface-contact constraint, the analytical expression of unique \mathbf{z}_s^b is

$$\begin{aligned} \mathbf{z}_s &= \pm \frac{\mathbf{t}_2 \times (\mathbf{q}_2 - \mathbf{q}_1)}{|\mathbf{t}_2 \times (\mathbf{q}_2 - \mathbf{q}_1)|} \text{ s.t. } -(\mathbf{z}_s)^T \mathbf{q}_1 = -(\mathbf{z}_s)^T \mathbf{q}_2 > 0 \\ \mathbf{z}_s^b &= \frac{-1}{\sqrt{2}} [c_{\phi_1}, -s_{\phi_2}, c_{\phi_2}]^T, \quad -(\mathbf{z}_s^b)^T \mathbf{q}_1 = -(\mathbf{z}_s^b)^T \mathbf{q}_2 = \frac{r}{\sqrt{2}} \end{aligned} \quad (8)$$

Case 3. Both tangent vectors \mathbf{t}_i defined: For this case, \mathbf{z}_s^b is normal to the plane containing vector Q_1Q_2 and tangent vectors at points Q_1 and Q_2 . Consequently, angles ϕ_i are

$$\begin{aligned} (\mathbf{q}_1 - \mathbf{q}_2)^T (\mathbf{t}_1 \times \mathbf{t}_2) &= 0 \\ \Rightarrow -r^3(s_{\phi_1} + s_{\phi_2}) &= 0 \Rightarrow \phi_2 = -\phi_1 \text{ or } 180^\circ + \phi_1 \end{aligned}$$

$$\phi_2 = \begin{cases} -\phi_1 & , \mathbf{z}_s^b = \frac{1}{\sqrt{2c_{\phi_1}^2 + s_{\phi_1}^2}} [c_{\phi_1}, s_{\phi_1}, c_{\phi_1}]^T \\ 180^\circ + \phi_1, \mathbf{z}_s^b = \frac{1}{\sqrt{2c_{\phi_1}^2 + s_{\phi_1}^2}} [c_{\phi_1}, s_{\phi_1}, -c_{\phi_1}]^T \end{cases} \quad (9)$$

This case is infeasible due to the range constraints on ϕ_1, ϕ_2 . More specifically, for $\phi_2 > 0$, both $-\phi_1$ and $180^\circ + \phi_1$ are outside of the solution space, i.e., the arc range $\phi_2 \in [0, 180^\circ]$.

E. Hybrid System

Given that the surface normal is defined only for cases 1 and 2, the robot can be modeled as a hybrid system transitioning between four states. Each state corresponds to the robot instantaneously pivoting about one endpoint.

State 1: $\phi_1 \in (0, 180^\circ), \phi_2 = 0^\circ$, A_2 pivot, roll along L_1

State 2: $\phi_1 \in (0, 180^\circ), \phi_2 = 180^\circ$, B_2 pivot, roll along L_1

State 3: $\phi_1 = 0^\circ, \phi_2 \in (0, 180^\circ)$, A_1 pivot, roll along L_2

State 4: $\phi_1 = 180^\circ, \phi_2 \in (0, 180^\circ)$, B_1 pivot, roll along L_2

As an example, the geometric representation of the robot in State 2 and pivoting about the endpoint B_2 where tangent

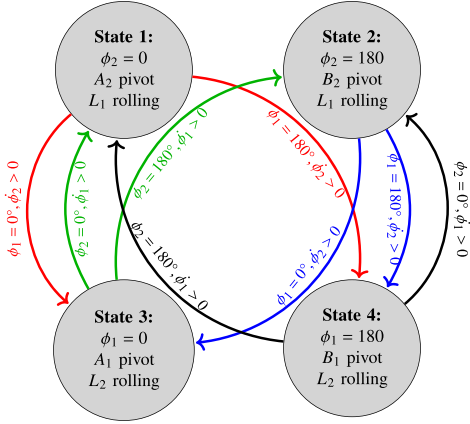


Fig. 3. Four state hybrid system model of TeXploR. The state transition is decided by the pivot and the rate of change of point of contact $\dot{\phi}_i$. During each state, the robot pivots about one of the ends of the curved-links while rolling about the other.

vector t_2 is not defined is shown in Fig. 2. TeXploR is a hybrid system transitioning between four states of locomotion. More importantly, all states are not connected to each other. For example, the robot cannot transition directly from State 1 to 2, instead the transition is $1 \rightarrow 3 \rightarrow 2$ or $1 \rightarrow 4 \rightarrow 2$. In each state, the transition occurs when ϕ_i is fixed at $0^\circ, 180^\circ$ and $\dot{\phi}_{i\pm 1} > 0$. The hybrid states are summarized in Fig. 3.

Let's analyze the transition between States $1 \rightarrow 3 \rightarrow 2 \rightarrow 4$: while in State 1, ϕ_1 reaches A_1 . The robot transitions to State 3 as $\phi_1 \rightarrow 0^\circ$ and pivots about A_1 while ϕ_2 begins to traverse L_2 . Next, it arrives at the $\phi_2 = 180^\circ$, i.e., B_2 . Now, with $\dot{\phi}_2 > 0$, and the robot transitions to State 2. Here, $\phi_2 = 180^\circ$ as ϕ_1 traverses L_1 , stopping at B_1 . Finally, it transitions to State 4. The robot repeatedly transitions between these states either forward or backwards for a rolling sequence.

F. Generalizability for Different Robot Morphologies

The extension of this framework to different curved-link tensegrities requires it to apply to systems with varying robot shape (T_{12}), number of curved-links, and curved-link lengths.

Shape morphing: Individual cable tensions have direct impact on robot shape, specifically the transformation matrix T_{12} defined in (2). Variations in the orientation and distance between the two curved-links has direct impact on the rolling path [17]. For this research, the curved-links are orthogonal with coincident arc centers. This enables a straight trajectory during a rolling sequence. Shape morphing, reflected in Fig. 4(a), enables turning. This change is incorporated by updating the point of contact and tangent vector as a function of \mathbf{o}_{12}, R_{12} .

$$\mathbf{q}_2 = \mathbf{o}_{12} + R_{12}\mathbf{q}_2^2, \quad t_2 = \frac{\partial \mathbf{q}_2}{\partial \phi_2}$$

Number of curved-links: The framework is adaptable to tensegrity robots with more curved-links, e.g., three as shown in Fig. 4(b). For this morphology, (6) will be modified to

$$[(\mathbf{q}_1 - \mathbf{q}_2) \quad (\mathbf{q}_2 - \mathbf{q}_3) \quad (\mathbf{t}_1) \quad (\mathbf{t}_2) \quad (\mathbf{t}_3)]^T \mathbf{z}_s = \mathbf{0} \quad (10)$$

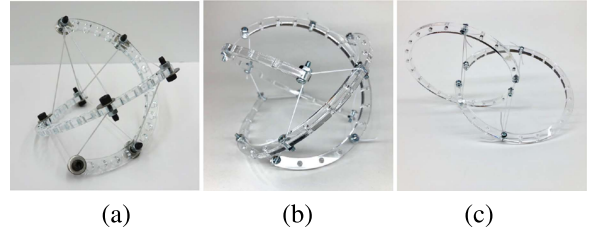


Fig. 4. Different robot morphologies that can be modeled with the generalizable framework: (a) A two link prototype with a different T_{12} . (b) Three curved-links resulting in three points of ground contact. (c) A two link prototype with arc length $> 180^\circ$.

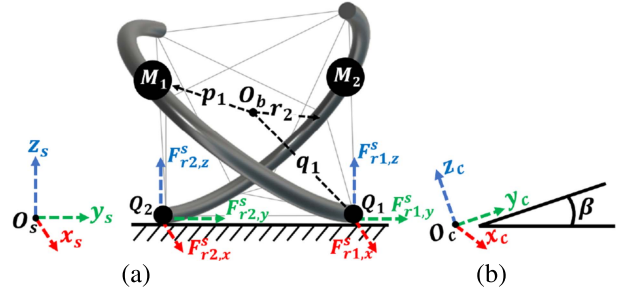


Fig. 5. (a) Free-body diagram of TeXploR with reaction forces. (b) Incline β with fixed reference coordinate system $\{c\}$.

where $\mathbf{q}_3, \mathbf{t}_3$ are defined for the new point of contact Q_3 on the third curved-link. Consequently, the analysis will result in a change in number of robot states in the hybrid system.

Curve-link length: The arc lengths of the curves can be varied beyond 180° as illustrated in Fig. 4(c). This alteration in the robot morphology will result in reconsideration of the possibility of a solution existing for ‘Case 3’ discussed in Section II-D. This may result in an increase in the number of robot states from the four discussed earlier.

III. STATIC MODELING

The two-point of contact, hybrid system nature results in four feasible states. Consequently, the analytical solution to statics is obtained by equating the wrench to zero and solving for the unique point of contact corresponding to the robot orientation.

A. Closed Form Solution for Point of Contact

The wrench, \mathcal{F} , is comprised of the total force, \mathbf{f} , and moment, \mathbf{m} , acting on the body. For the static formulation, the wrench \mathcal{F} about O_b is equated to zero. The corresponding free body diagram of the two point of contact system with the reaction forces $\mathbf{F}_{r1}, \mathbf{F}_{r2}$ at the points of contact are shown in Fig. 5. Here, the center of mass of the curved-links $r_1^b = r_2^b = [0, 2r/\pi, 0]^T$.

$$\begin{aligned} \mathcal{F} = \begin{bmatrix} \mathbf{f} \\ \mathbf{m} \end{bmatrix} &= \sum_{i=1}^2 \begin{bmatrix} (M_i + m_i)g\mathbf{z}_s + \mathbf{F}_{ri} \\ M_i g \dot{\mathbf{p}}_i \mathbf{z}_s + m_i g \hat{\mathbf{r}}_i \mathbf{z}_s + \hat{\mathbf{q}}_i \mathbf{F}_{ri} \end{bmatrix} = \mathbf{0} \quad \text{s.t.} \\ \mathbf{f}^s &= \begin{bmatrix} F_{r1,x}^s - F_{r2,x}^s \\ F_{r1,y}^s - F_{r2,y}^s \\ (M_1 + M_2 + m_1 + m_2)g - (F_{r1,z}^s + F_{r2,z}^s) \end{bmatrix} \end{aligned}$$

$$\mathbf{m}^b = \sum_{i=1}^2 \left(M_i g \hat{\mathbf{p}}_i^b + m_i g \hat{\mathbf{r}}_i^b - F_{ri,z}^s \hat{\mathbf{q}}_i^b \right) \mathbf{z}_s^b + \left(F_{r1,x}^s \hat{\mathbf{q}}_1^b - F_{r2,x}^s \hat{\mathbf{q}}_2^b \right) \mathbf{x}_s^b + \left(F_{r1,y}^s \hat{\mathbf{q}}_1^b - F_{r2,y}^s \hat{\mathbf{q}}_2^b \right) \mathbf{y}_s^b$$

These equations have seven unknowns $F_{ri,x}^s, F_{ri,y}^s, F_{ri,z}^s$ and ϕ_i along the rolling link for a corresponding state. This can be simplified to three unknowns $F_{r1,z}^s, F_{r2,z}^s, \phi_i$ by observing $F_{r1,x}^s = F_{r2,x}^s, F_{r1,y}^s = F_{r2,y}^s$, and $Q_1 Q_2$ lies in the same plane as $\mathbf{x}_s, \mathbf{y}_s$, i.e., $(\hat{\mathbf{q}}_1 - \hat{\mathbf{q}}_2) \mathbf{x}_b = (\hat{\mathbf{q}}_1 - \hat{\mathbf{q}}_2) \mathbf{y}_b = 0$. Hence,

$$\mathcal{F} = \sum_{i=1}^2 \left[\begin{pmatrix} (M_i + m_i)g - (F_{ri,z}^s) \\ (M_i g \hat{\mathbf{p}}_i^b + m_i g \hat{\mathbf{r}}_i^b - F_{ri,z}^s \hat{\mathbf{q}}_i^b) \end{pmatrix} \mathbf{z}_s^b \right] = 0$$

Using the calculated \mathbf{z}_s^b from Section II-D for each state, the ground contact angles and reaction forces are determined as
State 1: Pivot about A_2 ($\phi_2 = 0^\circ$), rolling on L_1

$$\begin{aligned} \mathbf{z}_s^b &= -\frac{1}{\sqrt{2}} [c_{\phi_1}, s_{\phi_1}, 1]^T, \quad \tan \phi_1 = \frac{s_{\theta_1} - s_{\theta_2}}{c_{\theta_1}} \\ F_{r1,z} &= Mg \left[-1 + \frac{c_{\phi_1+\theta_2}}{2} - c_{\theta_2} + c_{\phi_1-\theta_1} - \frac{c_{\phi_1-\theta_2}}{2} \right] - mg \\ F_{r2,z} &= Mg \left[-1 - \frac{c_{\phi_1+\theta_2}}{2} + c_{\theta_2} - c_{\phi_1-\theta_1} + \frac{c_{\phi_1-\theta_2}}{2} \right] - mg \end{aligned} \quad (11)$$

State 2: Pivot about B_2 ($\phi_2 = 180^\circ$), rolling on L_1

$$\begin{aligned} \mathbf{z}_s^b &= -\frac{1}{\sqrt{2}} [c_{\phi_1}, s_{\phi_1}, 1]^T, \quad \tan \phi_1 = \frac{s_{\theta_1} - s_{\theta_2}}{c_{\theta_1}} \\ F_{r1,z} &= Mg \left[-1 + \frac{c_{\phi_1+\theta_2}}{2} + c_{\theta_2} + c_{\phi_1-\theta_1} - \frac{c_{\phi_1-\theta_2}}{2} \right] - mg \\ F_{r2,z} &= Mg \left[-1 - \frac{c_{\phi_1+\theta_2}}{2} - c_{\theta_2} - c_{\phi_1-\theta_1} + \frac{c_{\phi_1-\theta_2}}{2} \right] - mg \end{aligned} \quad (12)$$

State 3: Pivot on A_1 ($\phi_1 = 0^\circ$), rolling about L_2 :

$$\begin{aligned} \mathbf{z}_s^b &= \frac{1}{\sqrt{2}} [-1, s_{\phi_2}, -c_{\phi_2}]^T, \quad \tan \phi_2 = \frac{s_{\theta_2} - s_{\theta_1}}{c_{\theta_2}} \\ F_{r1,z} &= Mg \left[-1 - \frac{c_{\phi_2+\theta_1}}{2} + c_{\theta_1} - c_{\phi_2-\theta_2} + \frac{c_{\phi_2-\theta_1}}{2} \right] - mg \\ F_{r2,z} &= Mg \left[-1 + \frac{c_{\phi_2+\theta_1}}{2} - c_{\theta_1} + c_{\phi_2-\theta_2} - \frac{c_{\phi_2-\theta_1}}{2} \right] - mg \end{aligned} \quad (13)$$

State 4: Pivot on A_2 ($\phi_1 = 180^\circ$), rolling about L_2 :

$$\begin{aligned} \mathbf{z}_s^b &= \frac{1}{\sqrt{2}} [-1, -s_{\phi_2}, c_{\phi_2}]^T, \quad \tan \phi_2 = \frac{s_{\theta_2} - s_{\theta_1}}{c_{\theta_2}} \\ F_{r1,z} &= Mg \left[-1 - \frac{c_{\phi_2+\theta_1}}{2} + c_{\theta_1} - c_{\phi_2-\theta_2} + \frac{c_{\phi_2-\theta_1}}{2} \right] - mg \\ F_{r2,z} &= Mg \left[-1 + \frac{c_{\phi_2+\theta_1}}{2} - c_{\theta_1} + c_{\phi_2-\theta_2} - \frac{c_{\phi_2-\theta_1}}{2} \right] - mg \end{aligned} \quad (14)$$

B. Rotation Matrix

As evident, the static analysis allows for closed form solution for \mathbf{z}_s^b . The equilibrium orientation does not provide any information about the planar position of the robot on the surface, i.e., x, y components of O_b are ‘free’ while the z component is fixed at $r/\sqrt{2}$ as calculated in (7), (8). Hence, ignoring additional

rotation about \mathbf{z}_s the rotation matrix can be calculated using the Rodrigues’ formula and vectors $\mathbf{z}_s, \mathbf{z}_s^b$

$$R_{sb}(\mathbf{u}, \theta) = I + \sin \theta \hat{\mathbf{u}} + (1 - \cos \theta) \hat{\mathbf{u}}^2$$

$$\text{where } \mathbf{u} = \frac{\mathbf{z}_s^b \times \mathbf{z}_s}{|\mathbf{z}_s^b \times \mathbf{z}_s|}, \quad \theta = \text{atan2}(|\mathbf{z}_s^b \times \mathbf{z}_s|, (\mathbf{z}_s^b)^T \mathbf{z}_s) \quad (15)$$

Rodrigues’ formula converts axis \mathbf{u} and angle θ into an $SO(3)$ rotation matrix. Additionally, $\mathbf{o}_{sb}^s = [x, y, \sqrt{r}/2]^T$ for some x, y , i.e., the robot can sit anywhere on the plane. A closed form solution for T_{sb} is obtained by combining R_{sb} and \mathbf{o}_{sb} .

C. Generalizability of Statics With Surface Friction or Inclines

When considering the Coulomb friction model, maximum friction force is proportional to the pressure of contact between two surfaces where μ is the coefficient of friction.

$$\sqrt{(F_{ri,x}^s)^2 + (F_{ri,y}^s)^2} \leq \mu |F_{ri,z}^s| \quad (16)$$

However, when the robot rests on an incline, the inequality must compensate for the change in the reaction force w.r.t. the surface normal. Let β be the angle between the incline surface and flat ground as shown in Fig. 5(b). The incline coordinate system $\{c\}$ is defined by orthonormal basis vectors $U_c = [\mathbf{x}_c, \mathbf{y}_c, \mathbf{z}_c] \in SO(3)$ where \mathbf{x}_c is parallel to the incline and \mathbf{z}_c is normal to the incline surface. It is important to remind the reader that the prior calculations of arc contact angle ϕ_i , surface normal \mathbf{z}_b^s , and the rotation matrix remain unaltered as the equations of motion remain the same. The friction constraint changes the coordinate system representation in (16) from $\{s\} \rightarrow \{c\}$ where the relationship between $\mathbf{F}_{ri}^s, \mathbf{F}_{ri}^c$ can be obtained from the principle that vectors are coordinate invariant.

$$\mathbf{F}_{ri} = U_s \mathbf{F}_{ri}^s = U_c \mathbf{F}_{ri}^c \Rightarrow \mathbf{F}_{ri}^c = \begin{bmatrix} 1 & 0 & 0 \\ 0 & c_\beta & s_\beta \\ 0 & -s_\beta & c_\beta \end{bmatrix} \mathbf{F}_{ri}^s \quad (17)$$

In the supplemental video, a surface incline of 5° is shown. Here, the static equilibrium position remains the same for 0° and 5° . We speculate that angles much higher than this would result in tip-over where the robot would begin to roll due to an imbalance on the net moment and forces causing a shift in the center of mass. This behaviour occurs when $F_{ri,z}^c < 0$. Additionally, although the robot orientation does not matter on a flat plane, it can alter the static stability, i.e., maximum achievable inclination angle. This is because the robot will come out of balance faster when aligned with the incline, making yaw an important parameter when balancing on inclines.

IV. TEXPLORER DESIGN AND FABRICATION

A. Static Form Finding

TeXploR is a tensegrity mechanism that combines elements of tension and compression. The fabrication of such robots is non-trivial due to the antagonistic elements involved. This section describes the form-finding approach to determine the cable lengths that are required to achieve the desired T_{12} from (2). This is performed by minimizing the energy of the system [21], [22]. We define the problem in terms of the generalized coordinates,

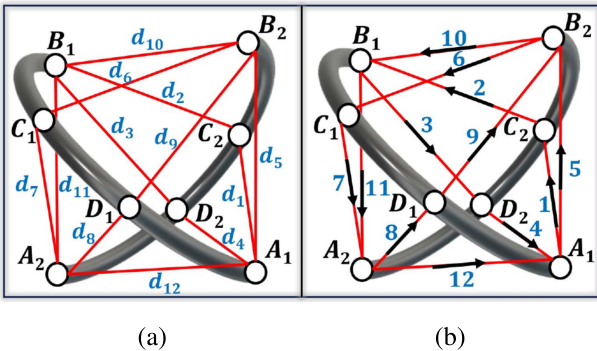


Fig. 6. (a) The twelve cables joining different points on the two curved-links are denoted by $d_j, j \in [1, 12]$. (b) The tendon routing path ensures that each edge is only traversed once.

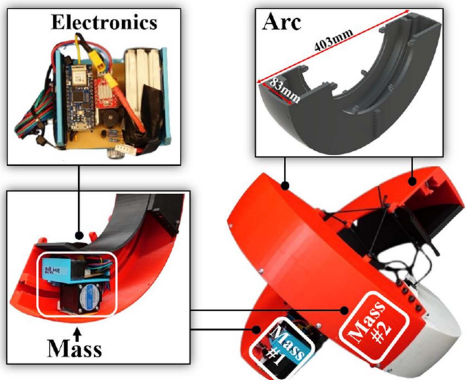


Fig. 7. TeXploR comprises of two arcs with 83 mm thickness and 403 mm diameter. The internal shifting masses (mechatronics) that move along a GT2 belt internal to each arc.

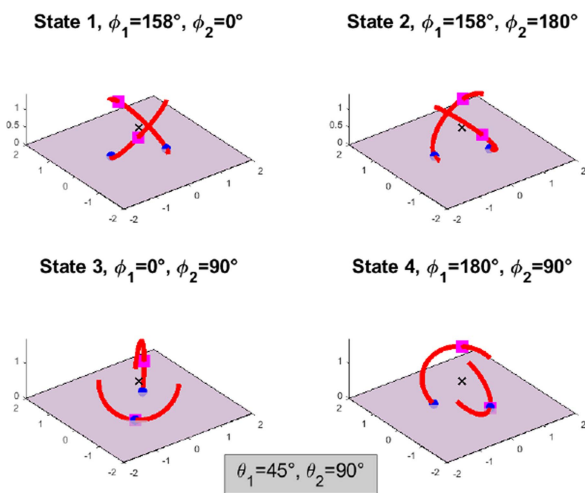


Fig. 8. Four static equilibrium solutions for ($\theta_1 = 45^\circ$, $\theta_2 = 90^\circ$). The blue dots are the points of contact q_i , the pink squares are the positions of the internal masses p_i , and the black 'x' represents origin O_b of the body coordinate system.

i.e., the screw ξ using a Lie groups approach. The four connection points on each curved-link are identical and expressed in the corresponding link coordinate systems. Consequently, the 12 cable segments are expressed as $D \in \mathbb{R}^{4 \times 12}$ where the i th

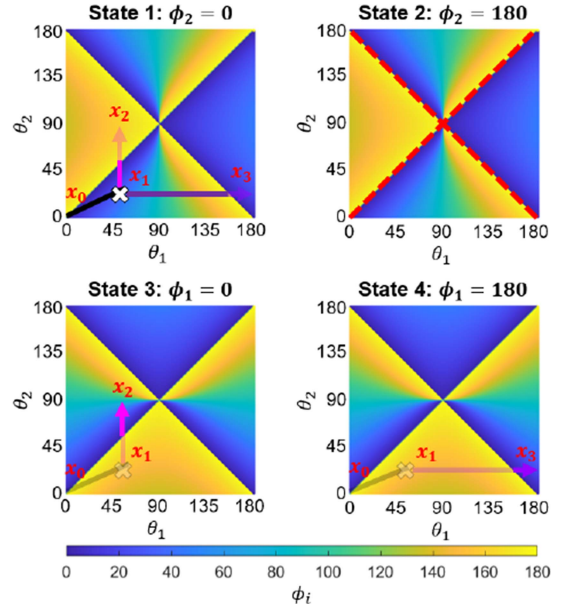


Fig. 9. Simulation of static equilibrium positions of the four states. Two quasi-static control path sequences highlight the state transition boundaries (dotted red line): $x_0 \rightarrow x_1 \rightarrow x_2$ for State 1 \rightarrow 3 and $x_0 \rightarrow x_1 \rightarrow x_3$ for State 1 \rightarrow 4.

cable d_i is denoted by the i th column.

$$P = \begin{bmatrix} p_A & p_B & p_C & p_D \\ 1 & 1 & 1 & 1 \end{bmatrix} = \begin{bmatrix} -r & 0 & 0 & 1 \\ \frac{-r}{2} & \frac{-\sqrt{3}r}{2} & 0 & 1 \\ \frac{r}{2} & \frac{\sqrt{3}r}{2} & 0 & 1 \\ r & 0 & 0 & 1 \end{bmatrix}^T$$

$$C^i[j, k] = \begin{cases} 1 & \text{if cable } k \text{ contains vertex } j \text{ on link } i \\ 0 & \text{otherwise} \end{cases}$$

$$D(\xi) = PC^1 - e^{\hat{\xi}} PC^2 = PC^1 - T_{12}PC^2$$

$$D = [d_1, d_2, \dots, d_{12}], \quad |d_i| = \sqrt{|d_{1,i}|^2 + \dots + |d_{4,i}|^2} \quad (18)$$

P is the concatenated homogeneous representation of points A_i, B_i, C_i, D_i on each arc in Fig. 6. The connectivity matrices $C^1, C^2 \in \mathbb{R}^{4 \times 12}$ mathematically represent the ends of each cable. The energy minimization problem is written as

$$\xi^* = \min_{\xi} \sum_{i=1}^{12} \frac{1}{2} k (|d_i| - d_{0,i})^2 \quad (19)$$

where $k, d_{0,i}$ are the stiffness and the free length of the corresponding cable measured not under tension. There are two different cable segments in the robot corresponding to edge-to-edge (e.g., d_{12}, d_5) and edge-to-middle segments (e.g., d_1, d_4) with free-length of 83 mm and 76 mm respectively, and the stiffness coefficient of 0.0497 N/m. The optimal $T_{12} = e^{\hat{\xi}}$ matches (2) with $d_1 = 149$ mm and $d_2 = 141$ mm in Fig. 6(a).

B. Tendon Routing

Routing the cable through the two arcs such that the mechanism maintains structural integrity is challenging given the antagonistic nature of tensile cables and compressive rigid

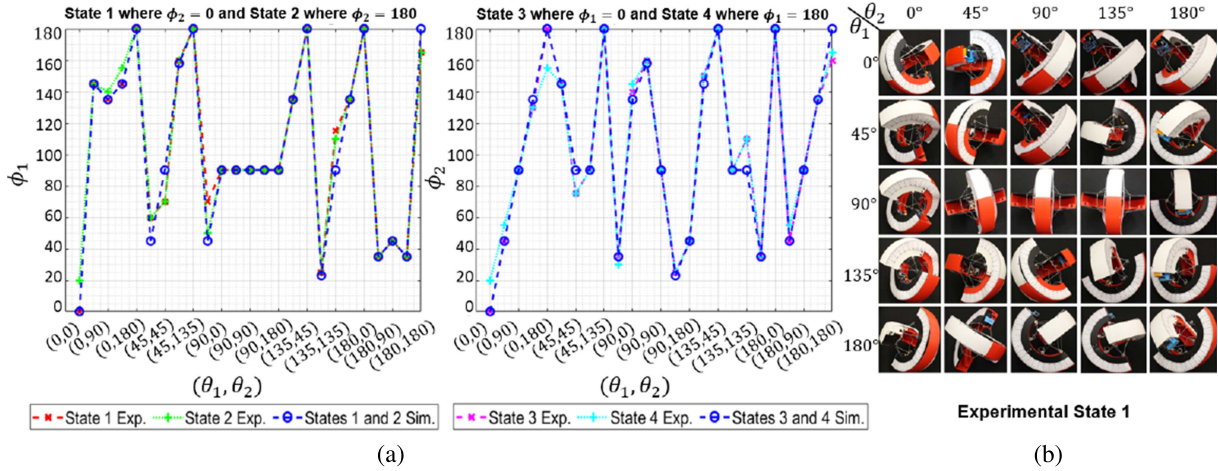


Fig. 10. Experimental static solutions are validated through incrementally varying (θ_1, θ_2) by 45° . (a) The experimental vs. simulated values for States 1-4. (b) All overhead experimental results for State 1.

curved-links. This is achieved by finding the Euler path of the graph where the connected edges and vertices correspond to the cables and connection points respectively. The reader may refer to [23] for more details. One such Euler path, $A_1 \rightarrow C_2 \rightarrow B_1 \rightarrow D_2 \rightarrow A_1 \rightarrow B_2 \rightarrow C_1 \rightarrow A_2 \rightarrow D_1 \rightarrow B_2 \rightarrow B_1 \rightarrow A_2 \rightarrow A_1$, is shown in Fig. 6(b). Here, the sequence simplifies the fabrication process by ensuring the cable traverses each edge only once. Once routed, the segments are tightened until the two curved-links are held in tension with the optimal cable lengths identified through form-finding.

C. Mechatronics

TeXploR is comprised of two 3D printed PLA arcs with 83 mm thickness and 403 mm diameter that are structurally held with a cable using the discussed routing approach. Motion is performed with a motor assembly traversing a GT2 timing belt running internally along the arc. A side view of an arc with the traveling mass is shown in Fig. 7. The motor assembly are all positioned to one side of the timing belt with supporting delrin sliders on the top and side to maintain track alignment during movement. An Arduino Nano33 IoT, A4988 motor driver, 1,100 mAh LiPo battery, and PCB are arranged atop the traveling NEMA17 stepper motor. Each semicircular arc weighs 431g while each shifting mass weighs 427g, resulting in a nearly 1:1 weight ratio. This allows incremental mass movements to have a large impact on the shifting body center of mass.

V. RESULTS

A. Simulation

Simulations are performed in MATLAB to obtain the robot equilibrium position. Given the internal mass positions (θ_1, θ_2) , the equilibrium position can be interpreted as the two points of contacts represented through ground contact angles (ϕ_1, ϕ_2) . These four states are analytically found using (11)–(14). As an example, Fig. 8 illustrates the four state solutions for internal mass positions $(\theta_1, \theta_2) = (45^\circ, 90^\circ)$. Here, the black cross, pink squares, and blue circles indicate the origin O_b of the body coordinate system, internal masses, and ground contact points.

The simulated ground contact angles for the four states as a function of the internal mass positions are shown in Fig. 9. As

evident from the analytical solutions, the ground contact angles for States (1, 2) and (3, 4) solutions are identical. The plots demarcate the solutions in four distinct quadrants separated by the state transition boundaries highlighted by the dotted red lines in State 2 of Fig. 9. When considering this state, the bottom and top quadrants result in more movement of the robot, i.e., greater change in ϕ_2 for change in (θ_1, θ_2) as compared to the left and right quadrants. The state transition boundaries represent the internal mass positions where the robot can switch states. Consider two movement sequences visualized in Fig. 9. The robot starts at internal mass position $x_0 = (0, 0)$ in State 1. Next, the internal masses are quasi-statically moved to position x_1 where ϕ_2 is fixed at 0° . Thereafter, the robot travels along a vertical path (θ_1 constant, θ_2 increasing) and approaches the state transition boundary where $\phi_1 \rightarrow 0^\circ$. Instantaneously the robot enters the left quadrant of State 3 and ϕ_2 begins to increase, rolling to position x_2 . The second movement again starts with the robot at position x_0 in State 1 rolling to x_1 , and then begins to move towards the right state transition boundary as $\phi_1 \rightarrow 180^\circ$. The robot transitions along the boundary and instantly enters the right quadrant of State 4, stopping at x_3 .

B. Real-World Experiments

The prototype shown in the supplemental video is used for experimental validation of the simulations. For (θ_1, θ_2) increments of 45° , the ground contact angles (ϕ_1, ϕ_2) corresponding to the robot orientation were observed. The model assumes pure rotation during internal mass shifting, and that was also achieved during the real-world testing. It is possible this assumption will not hold on inclines where slipping may occur, but that was not observed during testing. Protractor strips were attached along the curved-links for reading ground contact angles. All results were compared with simulation for each state in Fig. 10(a). For most inputs, the ϕ_i angles match exactly. The mean absolute error (MAE) over all inputs is 4.36° , showing that the differences between the physical prototype and the simulated model create minimal error. The factors contributing to the differences between real-to-sim can be attributed to the assumptions and simplifications in the model of the system as well as a minimal amount of human error that is introduced by the ground contact angle measurement method. More specifically, the curved-links

are modeled as 2D bars with a single ground contact point, but the prototype has an arc thickness of 83 mm with a curved-arc endpoint that may allow for a range of different x_s, y_s ground contact positions when a shifting mass is fixed at either endpoint. This can lead to a small difference in the other ground contact point. Although 4.36° MAE is an acceptable amount of error, we hypothesize there would be even less discrepancy between the prototype and simulated model with a thinner arc thickness. Additionally, the center of mass of each shifting mass is modeled as a point mass while the mechatronics of the shifting mass are not centered due to slightly uneven component layout. The results for each State 1 input are shown in Fig. 10(b).

VI. CONCLUSION

This research introduces a static modeling framework using geometric representation applicable to multi-point of contact systems. The holonomic constraints prove the hybrid nature of the piecewise continuous rolling robot existing in four states. Such multi-point contact system modeling is explored for the first time in literature and the hybrid state model is verified by the real-world behavior of the robot. Each state physically corresponds to pivoting about one endpoint of the curved-links while rolling along the other. The modeling framework is generalizable and extendable to similar platforms of varying morphologies: robots with different shape, greater number of curved-links, and varying curved-link length, or their combination. The static analysis yields a four quadrant relationship between internal mass positions and ground contact angles. The quadrants are separated by state transition boundaries. A quasi-static movement along these boundaries results in a change of state, i.e., change in pivot points. The model is validated on a tetherless prototype with a MAE of 4.36° , highlighting accuracy of the model. Future work involves dynamically modeling TeXploR with consideration of dynamic movement of the internal mass. Experimental validation will then be performed in unstructured environments to showcase the capabilities of curved-link tensegrity robots in real-world scenarios.

ACKNOWLEDGMENT

The authors would like to thank Chase Fortin for his help in fabricating several iterations of the prototype. Any opinions, findings, conclusions, or recommendations expressed in this material are those of the authors and do not necessarily reflect the views of NASA.

REFERENCES

- [1] K. G. Gim and J. Kim, "Ringbot: Monocycle robot with legs," *IEEE Trans. Robot.*, vol. 40, pp. 1890–1905, 2024.
- [2] U. Saranli, M. Buehler, and D. E. Koditschek, "RHex: A simple and highly mobile hexapod robot," *Int. J. Robot. Res.*, vol. 20, no. 7, pp. 616–631, 2001.
- [3] R. D. Quinn et al., "Parallel complementary strategies for implementing biological principles into mobile robots," *Int. J. Robot. Res.*, vol. 22, no. 3/4, pp. 169–186, 2003.
- [4] R. Chase and A. Pandya, "A review of active mechanical driving principles of spherical robots," *Robotics*, vol. 1, no. 1, pp. 3–23, Dec. 2012. [Online]. Available: <https://www.mdpi.com/2218-6581/1/1/3>
- [5] A. Morinaga, M. Svinin, and M. Yamamoto, "A motion planning strategy for a spherical rolling robot driven by two internal rotors," *IEEE Trans. Robot.*, vol. 30, no. 4, pp. 993–1002, Aug. 2014.
- [6] T. Ohsawa, "Geometric kinematic control of a spherical rolling robot," *J. Nonlinear Sci.*, vol. 30, no. 1, pp. 67–91, Feb. 2020. [Online]. Available: <http://link.springer.com/10.1007/s00332-019-09568-x>
- [7] K. Snelson, "Snelson on the tensegrity invention," *Int. J. Space Struct.*, vol. 11, no. 1/2, pp. 43–48, 1996.
- [8] R. E. Skelton and M. C. De Oliveira, *Tensegrity Systems*, vol. 1, New York: Springer, 2009.
- [9] C. Paul, F. Valero-Cuevas, and H. Lipson, "Design and control of tensegrity robots for locomotion," *IEEE Trans. Robot.*, vol. 22, no. 5, pp. 944–957, Oct. 2006.
- [10] A. P. Sabelhaus et al., "System design and locomotion of SUPERball, an untethered tensegrity robot," in *Proc. 2015 IEEE Int. Conf. Robot. Automat.*, Seattle, WA, USA, May 2015, pp. 2867–2873.
- [11] K. Caluwaerts et al., "Design and control of compliant tensegrity robots through simulation and hardware validation," *J. Roy. Soc. Interface*, vol. 11, no. 98, Sep. 2014, Art. no. 20140520. [Online]. Available: <https://royalsocietypublishing.org/doi/10.1098/rsif.2014.0520>
- [12] L.-H. Chen et al., "Soft spherical tensegrity robot design using rod-centered actuation and control," *J. Mechanisms Robot.*, vol. 9, Mar. 2017, Art. no. 025001, doi: [10.1115/1.4036014](https://doi.org/10.1115/1.4036014).
- [13] J. Rieffel and J.-B. Mouret, "Adaptive and resilient soft tensegrity robots," *Soft Robot.*, vol. 5, no. 3, pp. 318–329, 2018.
- [14] T. Rhodes, C. Gotberg, and V. Vikas, "Compact shape morphing tensegrity robots capable of locomotion," *Front. Robot. AI*, vol. 6, 2019, Art. no. 111. [Online]. Available: <https://www.frontiersin.org/articles/10.3389/frobt.2019.00111>
- [15] V. Böhm, T. Kaufhold, F. Schale, and K. Zimmermann, "Spherical mobile robot based on a tensegrity structure with curved compressed members," in *Proc. 2016 IEEE Int. Conf. Adv. Intell. Mechatron.*, Jul. 2016, pp. 1509–1514.
- [16] V. Böhm, T. Kaufhold, I. Zeidis, and K. Zimmermann, "Dynamic analysis of a spherical mobile robot based on a tensegrity structure with two curved compressed members," *Arch. Appl. Mechan.*, vol. 87, no. 5, pp. 853–864, May 2017, doi: [10.1007/s00419-016-1183-z](https://doi.org/10.1007/s00419-016-1183-z).
- [17] T. Kaufhold, F. Schale, V. Böhm, and K. Zimmermann, "Indoor locomotion experiments of a spherical mobile robot based on a tensegrity structure with curved compressed members," in *Proc. 2017 IEEE Int. Conf. Adv. Intell. Mechatron.*, Jul. 2017, pp. 523–528.
- [18] P. Schorr et al., "Kinematic analysis of a rolling tensegrity structure with spatially curved members," *Meccanica*, vol. 56, no. 4, pp. 953–961, Apr. 2021, doi: [10.1007/s11012-020-01199-x](https://doi.org/10.1007/s11012-020-01199-x).
- [19] M. Antali and G. Stepan, "Slipping–rolling transitions of a body with two contact points," *Nonlinear Dyn.*, vol. 107, no. 2, pp. 1511–1528, Jan. 2022, doi: [10.1007/s11071-021-06538-5](https://doi.org/10.1007/s11071-021-06538-5).
- [20] R. M. Murray, Z. Li, and S. S. Sastry, *A Math. Introduction to Robot. Manipulation*, 1st ed. Boca Raton, FL, USA: CRC Press, Dec. 2017. [Online]. Available: <https://www.taylorfrancis.com/books/9781351469791>
- [21] A. Tibert and S. Pellegrino, "Review of form-finding methods for tensegrity structures," *Int. J. Space Struct.*, vol. 18, no. 4, pp. 209–223, Dec. 2003, doi: [10.1260/026635103322987940](https://doi.org/10.1260/026635103322987940).
- [22] R. Connelly and W. Whiteley, "Second-order rigidity and prestress stability for TensegrityFrameworks," *SIAM J. Discrete Math.*, vol. 9, no. 3, pp. 453–491, Aug. 1996, doi: [10.1137/S0895480192229236](https://doi.org/10.1137/S0895480192229236).
- [23] C. Woods and V. Vikas, "Design and modeling framework for DexTeR: Dexterous continuum tensegrity manipulator," *J. Mechanisms Robot.*, vol. 15, Mar. 2023, Art. no. 031006, doi: [10.1115/1.4056959](https://doi.org/10.1115/1.4056959).